Real Gas and Surface Ablation Effects on Hypersonic Boundary Layer Instability over a Blunt Cone

Clifton H. Mortensen* and Xiaolin Zhong†

University of California, Los Angeles, California, 90095, USA

The objective of this research is to analyze the hypersonic boundary layer transition process where surface ablation is included using direct numerical simulation and linear stability theory. There has been little research into surface ablation effects on hypersonic boundary layer instability and the understanding of real gas effects on hypersonic boundary layer instability still contains uncertainties. In this paper linear stability theory calculations will be performed to analyze hypersonic boundary layer instability with surface ablation effects. A thermochemical nonequilibrium linear stability theory code with a gas phase model that includes multiple carbon species as well as a linearized surface ablation model is developed and validated. As there are strong near wall gradients in ablative flows a high-order method for discretizing the linear stability equations is given which can easily include high-order boundary conditions. The developed linear stability code along with a high-order shock-fitting method for hypersonic flows with thermochemical nonequilibrium and surface chemistry boundary conditions for graphite ablation are used to study hypersonic boundary layer stability for a 7° half angle blunt cone at Mach 15.99. Five separate meanflow simulations were run with the same geometry and freestream conditions to help separate real gas effects, blowing effects, and carbon species effects on hypersonic boundary layer instability. An N factor comparison shows that real gas effects significantly destabilize the flow when compared to an ideal gas. Carbon species resulting from ablation slightly destabilize the flow by increasing the amplification rate of linear disturbances. Blowing is destabilizing for the real gas simulation and has a negligible effect for the ideal gas simulation due to the different locations of instability onset.

Nomenclature

$\dot{m}$	Mass flux per area, kg/m^2· s
c_r	Phase speed, m/s
c_s	Mass fraction of species s
$c_{v,s}$	Species translation-rotation heat capacity at constant volume, J/kg· K
e	Specific total energy, J/kg
$e_{v,s}$	Species specific vibration energy, J/kg
e_v	Specific vibration energy, J/kg
h_s^o	Species heat of formation, J/kg
M_s	Species molecular weight, kg/mol
nms	Number of molecular species
ns	Number of species
$Q_{T-V,s}$	Species vibration energy transfer rate, J/m^3·s
R	Universal gas constant, 8.3143 J/mol· K
s	Surface streamline
T	Translation-rotation temperature, K
T_V	Vibration temperature, K
u_j	Velocity in jth direction, m/s
X_s	Molar concentration of species s, mol/m^3

Subscripts

∞	Freestream
s	Species
w	Wall

Symbols

α_r	Wavenumber, 1/m
-α_i	Growth rate, 1/m
δ_{ij}	Kronecker delta
μ	Viscosity, kg/m·s
ω_s	Rate of species production, kg/m^3·s
ρ	Density, kg/m^3

*Graduate Student, Mechanical and Aerospace Engineering, cmort22@gmail.com, AIAA Student Member.

†Professor, Mechanical and Aerospace Engineering, xiaolin@seas.ucla.edu, AIAA Associate Fellow.

I. Introduction

Thermal protection systems (TPS) are commonly used to protect hypersonic vehicles from the harsh high enthalpy environment they operate in.[1] Often a TPS is ablating such as those made using graphite or phenolic impregnated carbon ablator. Examples include nose cones or fins for thermal protection of hypersonic missiles and more recently SpaceX's Dragon capsule's heat shield. The design of these thermal protection systems is of major concern to the vehicle designer who must ensure the structural integrity of the vehicle throughout its flight envelope. Experimental testing of the various designs can be done in the laboratory or by flight tests. However the ground based simulation of the exact hypersonic flow conditions encountered in free flight may not be possible and free flight data does not yield the behavior of the entire flow field. Thus, numerical simulations play an important role as a complement to laboratory and flight test research as free flight conditions can be replicated and the entire flow field can be resolved.

A major consideration when evaluating the effectiveness of a TPS is estimation of boundary layer transition which has a strong effect on surface heating rates. If boundary layer transition can be estimated accurately it can help the thermal protection designer minimize the TPS safety factor and thus the vehicle weight. It is commonly understood that for flat plates and straight cones in a low disturbance environment the amplification of linear wavelike disturbances such as the second mode for hypersonic flows can lead to parametric instabilities and mode interactions and then to breakdown and finally turbulence. Eigenmode growth of linear wavelike disturbances is generally the slowest part of the transition process and the most unstable frequencies persist downstream. This makes the eigenmode growth region essential to understanding hypersonic boundary layer transition. Common methods for modeling these linear wavelike disturbances are linear stability theory (LST), parabolized stability equations (PSE), and direct numerical simulation (DNS). These methods are designed to predict the growth or decay of wavelike disturbances based on a laminar meanflow profile. This research focuses on LST to study real gas effects and ablation induced outgassing effects on hypersonic boundary layer stability over a blunt cone.

Significant research on the linear stability of boundary layers has been performed by Mack.[2] Mack found that the major instability waves for hypersonic boundary layers with a perfect gas assumption are the first and second modes. Following researchers have implemented numerical codes using linear stability theory to compute the most unstable frequencies for a variety of flow conditions and gas models. Malik[3] implemented multiple numerical methods for linear stability of perfect gas boundary layer flows. Most research on hypersonic boundary layer stability has used a perfect gas model and few researchers have studied effects of thermochemical nonequilibrium. Chang et al.[4] comment on real gas effects stating that it is "very important to account for the chemistry effect in future transition for hypersonic vehicles." Stuckert and Reed,[5] Hudson et al.,[6,7] Chang et al.[4] and Johnson et al.[8] studied boundary layer stability in nonequilibrium chemically reacting hypersonic boundary layers using linear stability theory. It was found that dissociation of air species is destabilizing to the second mode and stabilizing to the first mode. Ma and Zhong[9] studied the receptivity of free stream disturbances using DNS for a Mach 10 nonequilibrium oxygen flow over a flat plate. They found that in a Mach 10 oxygen flow there is a significant real gas destabilizing effect on the second-mode waves. However they did not consider thermal nonequilibrium or any gas/surface interaction.

Currently there has been a limited amount of numerical research on how ablation and surface chemistry models effect hypersonic boundary layer receptivity and stability. Johnson et al.[10] used linear stability analysis to analyze non-reacting and reacting hypersonic boundary layer stability with blowing and suction. Ghaffari et al.[11] performed a linear stability analysis of a hypersonic perfect gas flat plate boundary layer with wall blowing and found that as blowing increases the maximum amplification rate of the disturbance instability grows and moves to lower frequencies. Li et al.[12] studied boundary layer instability mechanisms for hypersonic perfect gas flows over slender cones and blunt capsules at zero angle of attack and an angle of attack of 16°. They found that for the slender cone out-gassing is moderately stabilizing to the second mode and for the blunt capsule out-gassing is destabilizing to the first mode. One major difference between previous research and what is presented here is commonly previous blowing profiles have been rather artificial i.e. from a similarity solution or set at random. Here the blowing profile is computed from a surface chemistry model which more accurately simulates an ablative type blowing profile.

This paper is an extension of previous research described in Ref. 13 and Ref. 14. In Ref. 13 a thermochemical nonequilibrium DNS code with boundary conditions to approximate graphite ablation was validated and initial unsteady findings were presented. In Ref. 14 a new thermochemical nonequilibrium LST code including carbon species due to graphite ablation was developed and compared with unsteady DNS results. While the gas phase models with carbon species were implemented the linearization of the gas/surface model

was still incomplete. Also, unsteady DNS results were given that showed a real gas simulation with surface ablation was significantly destabilized compared to a perfect gas simulation. While there was a large difference between the two flow types it was difficult to pinpoint the exact cause of the difference.

The goal of this paper is twofold: 1) to develop and validate a linearized surface ablation model included into a linear stability code and 2) to study real gas effects, blowing effects, and carbon species effects on hypersonic boundary layer stability over a blunt cone using the developed linear stability theory code. A thermochemical nonequilibrium linear stability theory code is required to help analyze boundary layer waves such as identifying the fast and slow modes as well as quickly identifying unstable frequencies. A linearized ablation model is required in the LST code to accurately compare to DNS simulations of graphite ablation. While the DNS code is used to compute the meanflow profiles the unsteady DNS computations for all of the separate meanflows are not yet available so instabilities will be computed using LST only. Ref 14 gives the most recent DNS simulations for the ablative meanflow and ideal gas meanflows. A simplified approach to ablation prediction is used to help keep the research focus on hypersonic boundary layer stability. An eleven species gas model is used to model chemical nonequilibrium. It contains a standard five species air model (N_2, O_2, NO, N, O). The remaining species contain carbon (C_3, CO_2, C_2, CO, CN, C) and are obtained from sublimation, oxidation, and ablation product reactions. A two-temperature model is used to simulate thermal nonequilibrium. Only graphite ablation is considered without the effects of charring, pyrolysis, surface recession and ablation induced roughness. The surface reactions considered contain oxidation, recombination of atomic oxygen and sublimation. A surface mass balance is used to set species mass fractions at the surface and temperature profiles within the ablator are not computed.

The paper will start with an overview of the governing equations and the gas phase models followed by the numerical methods for both the DNS and LST codes. An overview of the surface chemistry model as well as the linearized surface chemistry model will then given. After which the LST code with the linearized ablation model will be validated with unsteady data from the DNS code which was previously validated in Ref. 13. After validation, stability characteristics of a 7^o half angle blunt cone at Mach 15.99 will be computed to assess real gas effects, blowing effects, and carbon species effects on hypersonic boundary layer instability.

II. Governing Equations and Gas Phase Models

The governing equations for thermochemical nonequilibrium are formulated for a two-temperature model with the rotational energy mode assumed to be fully excited and eleven non-ionizing species with finite rate chemistry. Two temperatures are used to represent translation-rotation energy and vibration energy. The eleven species model (N_2, O_2, NO, C_3, CO_2, C_2, CO, CN, N, O, C) is used to simulate air, surface reactions, and reactions of air with ablation products. The conservative three-dimensional Navier-Stokes equations consist of eleven species mass conservation equations, three momentum conservation equations, the vibration energy conservation equation and the total energy conservation equation. Wang and Zhong,[15] Prakash et al.[16] and Mortensen and Zhong[13] have used similar formulations for shock-fitting DNS of thermochemical nonequilibrium flow. For both LST and DNS the governing equations as well as the gas phase models are the same. Written in vector form the governing equations are

$$\frac{\partial U}{\partial t} + \frac{\partial F_j}{\partial x_j} + \frac{\partial G_j}{\partial x_j} = W \tag{1}$$

where U is the state vector of conserved quantities and W is the source terms defined by

$$U = \begin{bmatrix} \rho_1 \\ \vdots \\ \rho_{ns} \\ \rho u_1 \\ \rho u_2 \\ \rho u_3 \\ \rho e \\ \rho e_v \end{bmatrix}, \quad W = \begin{bmatrix} \omega_1 \\ \vdots \\ \omega_{ns} \\ 0 \\ 0 \\ 0 \\ 0 \\ \sum_{s=1}^{nms} \left(Q_{T-V,s} + \omega_s e_{v,s} \right) \end{bmatrix}.$$

F_j and G_j are the inviscid and viscous fluxes respectively and are defined by

$$F_j = \begin{bmatrix} \rho_1 u_j \\ \vdots \\ \rho_{ns} u_j \\ \rho u_1 u_j + p\delta_{1j} \\ \rho u_2 u_j + p\delta_{2j} \\ \rho u_3 u_j + p\delta_{3j} \\ (\rho e + p)\, u_j \\ \rho e_v u_j \end{bmatrix}, \quad G_j = \begin{bmatrix} \rho_1 v_{1j} \\ \vdots \\ \rho_{ns} v_{nsj} \\ \tau_{1j} \\ \tau_{2j} \\ \tau_{3j} \\ -u_i\tau_{ij} - k_T \frac{\partial T}{\partial x_j} - k_V \frac{\partial T_V}{\partial x_j} + \sum_{s=1}^{nms} \rho_s h_s v_{sj} \\ -k_V \frac{\partial T_V}{\partial x_j} + \sum_{s=1}^{nms} \rho_s e_{v,s} v_{sj} \end{bmatrix}$$

where $v_{sj} = u_{sj} - u_j$ is the species diffusion velocity and $\tau_{ij} = \mu\left(\frac{\partial u_i}{\partial x_j} + \frac{\partial u_j}{\partial x_i}\right) - \frac{2}{3}\mu\frac{\partial u_k}{\partial x_k}\delta_{ij}$ is the viscous stress. The total energy per unit volume, ρe, is defined by

$$\rho e = \sum_{s=1}^{ns} \rho_s c_{v,s} T + \rho e_v + \frac{1}{2}\rho\left(u_1^2 + u_2^2 + u_3^2\right) + \sum_{s=1}^{ns} \rho_s h_s^{\circ} \tag{2}$$

where h_s° is the heat of formation of species s and $c_{v,s}$ is the species translation-rotation specific heat at constant volume defined as

$$c_{v,s} = \begin{cases} \frac{5}{2}\frac{R}{M_s}, & s = 1, 2, \ldots, nms \\ \frac{3}{2}\frac{R}{M_s}, & s = nms+1, \ldots, ns. \end{cases} \tag{3}$$

The vibration energy per unit volume, ρe_v, is defined as

$$\rho e_v = \sum_{s=1}^{nms} \rho_s e_{v,s} = \sum_{s=1}^{nms} \rho_s \left(\sum_{m=1}^{nmod} \frac{g_{s,m} R}{M_s} \frac{\theta_{v,s,m}}{\exp\left(\theta_{v,s,m}/T_V\right) - 1} \right) \tag{4}$$

where *nmod* refers to the number of vibrational modes for each polyatomic molecule, $\theta_{v,s,m}$ refers to the characteristic temperature of each vibrational mode, and $g_{s,m}$ is the degeneracy of each vibrational mode. For the diatomic species there is only one vibrational mode and the degeneracy is unity. For C_3 and CO_2 there are three vibrational modes where two modes have a degeneracy of unity and one has a degeneracy of two. The characteristic vibration temperatures and their degeneracies were taken from Park[17] for N_2, O_2 and NO, from Dolton et al.[18] for C_3, and from McBride[19] for CO_2, C_2, CO, and CN.

To model chemical nonequilibrium eight dissociation reactions and sixteen exchange reactions are used. Each reaction is governed by a forward and backward reaction rate determined by Eqs. (5) and (6) respectively. The forward reaction rates and constants are obtained Park,[20] Bhutta & Lewis[21] and Park et al.[22] The equilibrium coefficient, K_{eq}, is computed in two different ways. The first is a curve fit from Park[17] as in Eq. (7). The second is from the Gibbs Free energy approach where curve fits to the Gibbs Free energy are obtained from McBride et al.[19] as in Eqs. (8) and (9) respectively.

$$k_f = C_f T_a^{\eta} e^{(-\theta_d/T_a)} \tag{5}$$

$$k_b = k_f / K_{eq} \tag{6}$$

$$K_{eq} = A_0 \exp\left(\frac{A_1}{Z} + A_2 + A_3 \ln(Z) + A_4 Z + A_5 Z^2\right), \quad Z = \frac{10000}{T} \tag{7}$$

$$\frac{G^{\circ}}{RT} = a_1(1 - \ln T) - \frac{a_2}{2}T - \frac{a_3}{6}T^2 - \frac{a_4}{12}T^3 - \frac{a_5}{20}T^4 + \frac{a_6}{T} - a_7 \tag{8}$$

$$K_{eq} = \exp\left(-\frac{G^{\circ}}{RT}\right)(R_u T)^{-\Delta n} \tag{9}$$

To calculate the source term in the vibration energy equation representing the exchange of energy between the translation-rotation and vibration energies the Landau-Teller formulation is used

$$Q_{T-V,s} = \rho_s \frac{e_{v,s}(T) - e_{v,s}(T_V)}{< \tau_s > + \tau_{cs}} \tag{10}$$

where $< \tau_s >$ is the Landau-Teller vibration relaxation time given by Lee.[23] τ_{cs} is from Park[17] to more accurately model the relaxation time in areas of high temperatures occurring just downstream of the bow shock.

The viscosity of each species is computed using a Blottner curve fit shown in Eq. (11). The coefficients are obtained from Blottner,[24] Gupta,[25] and Candler.[26] The mixture viscosity is then found using each species viscosity from a mixing rule obtained from Wilke[27] (Eq. (12)). The total heat conductivities for each energy mode are computed in a similar fashion as viscosity. The diffusion velocity is calculated using Fick's law and a constant Schmidt number of 0.5.

$$\mu_s = 0.1 \exp\left[\left(A_s^\mu \ln\left(T\right) + B_s^\mu\right) \ln\left(T\right) + C_s^\mu\right] \tag{11}$$

$$\mu = \sum_{s=1}^{ns} \frac{X_s \mu_s}{\phi_s} \tag{12}$$

III. Numerical Method

A. DNS Numerical Method

A high-order shock-fitting method developed for perfect gas flow by Zhong[28] has been extended for use on thermochemical nonequilibrium flows to compute the flow field between the shock and the body. For shock-fitting computations the shock location is not known *a priori* so its position is solved along with the flow field. Since the shock position is not stationary the grid used to compute the flow field is a function of time. This leads to the coordinate transformation

$$\begin{cases} \xi = \xi(x,y,z) \\ \eta = \eta(x,y,z,t) \\ \zeta = \zeta(x,y,z) \\ \tau = t \end{cases} \iff \begin{cases} x = x(\xi,\eta,\zeta,\tau) \\ y = y(\xi,\eta,\zeta,\tau) \\ z = z(\xi,\eta,\zeta,\tau) \\ t = \tau \end{cases}$$

where η is normal to the body, ξ is in the streamwise direction, ζ is in the transverse direction, $\zeta_t = 0$ and $\xi_t = 0$. The governing equation can then be transformed into computational space as

$$\frac{1}{J}\frac{\partial U}{\partial \tau} + \frac{\partial E'}{\partial \xi} + \frac{\partial F'}{\partial \eta} + \frac{\partial G'}{\partial \zeta} + \frac{\partial E'_v}{\partial \xi} + \frac{\partial F'_v}{\partial \eta} + \frac{\partial G'_v}{\partial \zeta} + U\frac{\partial (1/J)}{\partial \tau} = \frac{W}{J} \tag{13}$$

where J is the Jacobian of the coordinate transformation and

$$E' = \frac{F_1\xi_x + F_2\xi_y + F_3\xi_z}{J} \tag{14}$$

$$F' = \frac{F_1\eta_x + F_2\eta_y + F_3\eta_z}{J} \tag{15}$$

$$G' = \frac{F_1\zeta_x + F_2\zeta_y + F_3\zeta_z}{J} \tag{16}$$

$$E'_v = \frac{G_1\xi_x + G_2\xi_y + G_3\xi_z}{J} \tag{17}$$

$$F'_v = \frac{G_1\eta_x + G_2\eta_y + G_3\eta_z}{J} \tag{18}$$

$$G'_v = \frac{G_1\zeta_x + G_2\zeta_y + G_3\zeta_z}{J}. \tag{19}$$

A seven point stencil is used to discretize the spatial derivatives

$$\frac{df_i}{dx} = \frac{1}{hb_i}\sum_{k=-3}^{3} \alpha_{i+k} f_{i+k} - \frac{\alpha}{6!b_i} h^5 \left(\frac{\partial f^6}{\partial^6 x}\right) \tag{20}$$

where

$$a_{i\pm3} = \pm 1 + \frac{1}{12}\alpha, \qquad a_{i\pm2} = \mp 9 - \frac{1}{2}\alpha \tag{21}$$

$$a_{i\pm1} = \pm 45 + \frac{5}{4}\alpha, \qquad a_i = -\frac{5}{3}\alpha \tag{22}$$

$$b_i = 60 \tag{23}$$

and where $\alpha < 0$ is a fifth order upwind explicit scheme and $\alpha = 0$ reduces to a sixth order central scheme. Here the inviscid terms use $\alpha = -6$ which yields a low dissipation fifth order upwinded difference and the viscous terms are discretized using $\alpha = 0$. Flux splitting is used for the inviscid flux terms and to compute second derivatives the first order derivative operator is applied twice.

Conditions behind the shock are calculated from Rankine-Hugoniot relations. In the freestream the flow is assumed to be in thermal equilibrium and the chemical composition of the flow is frozen. The shock is assumed to be infinitely thin which means that the flow has no time to relax as it crosses the shock as relaxation rates are finite. This leads to the chemical composition remaining constant across the shock as well as the vibration temperature. Since neither process has any time to relax across the shock the relaxation zone is entirely downstream of the shock. A complete derivation of thermochemical nonequilibrium shock fitting can be found from Prakash et al.[29]

B. LST Numerical Method

The derivation of the thermochemical nonequilibrium LST equations follows the work of Hudson[7] excepting the species velocity terms which are substituted into the governing equations before linearization similar to Klentzman et al.[30] The LST equations are derived from the governing equations (Eq. (1)) where the instantaneous flow is comprised of a mean and fluctuating component $q = \bar{q} + q'$. Here q represents any flow variable such as velocity, density, temperature, etc. The instantaneous flow is then substituted into the governing equations where the steady flow is assumed to satisfy the governing equations and is subtracted out. The meanflow is assumed to be a function of the wall normal coordinate y only i.e. $\bar{q}(x, y, z) \approx \bar{q}(y)$ and the flow disturbances are assumed to be small i.e. linear. The perturbations are then assumed to be in the form of a normal mode described by

$$q'(x, y, z) = \hat{q}(y) \exp\left[i\left(\alpha x + \beta z - \omega t\right)\right] \tag{24}$$

where ω is the circular frequency of the disturbance and α and β are the wavenumbers. Commonly ω and β are assumed to be real and the wavenumber α is assumed to be complex which means the disturbances grow in space rather than time. If ω is complex and α and β are real then the disturbances grow in time rather than space. For comparison to direct numerical simulation the spatial stability approach is used i.e. α is complex which results in the dispersion relation $\alpha = \Omega(\omega, \beta)$. Substituting in the normal mode form for the perturbations reduces the problem to a coupled set of ns+5 ordinary differential equations

$$\left(\mathbf{A}\frac{d^2}{dy^2} + \mathbf{B}\frac{d}{dy} + \mathbf{C}\right)\vec{\phi} = \vec{0} \tag{25}$$

where $\vec{\phi} = \{\hat{\rho}_1, \hat{\rho}_2, ..., \hat{\rho}_{ns}, \hat{u}, \hat{v}, \hat{w}, \hat{T}, \hat{T}_V\}^T$ and $\mathbf{A}$, $\mathbf{B}$ and $\mathbf{C}$ are complex square matrices of size ns+5. This is now a boundary value problem where the derivative operators can be discretized and the equations solved numerically.

For hypersonic compressible boundary layers it is important to have high grid resolution near the generalized inflection point.[2] The current computational grid is used to cluster grid points around the inflection point and has been used by previous researchers.[6] It is defined so

$$y = \frac{a\eta}{b - \eta} \tag{26}$$

where

$$a = \frac{y_{max} y_i}{(y_{max} - 2y_i)} \tag{27}$$

$$b = 1 + \frac{a}{y_{max}} \tag{28}$$

and y_{max} is the outer domain boundary, y_i is the location of the generalized inflection point and η runs from zero to one. For a cone frustum a generalized inflection point may not exist so y_i is placed near the boundary layer edge. If grid metrics are required they can be computed directly from Eq. (26).

With the grid defined, it is now possible to discretize the derivative operators. Malik[3] gives an excellent overview of numerical methods suitable for stability calculations of hypersonic flows which include finite difference, compact difference, and spectral formulations. A fourth order central difference scheme has been used by previous researchers[7,31] to good effect. Here a different approach than what has previously been used for hypersonic stability calculations is taken. The first and second derivative operators in the wall normal direction are discretized by taking derivatives of Lagrange polynomials in physical space. If x_p is the grid point where a first derivative is required then

$$\left.\frac{\partial f}{\partial x}\right|_{x_p} = \sum_{i=1}^{N} A_i f_i \tag{29}$$

where

$$A_i = \frac{\sum\limits_{\substack{j=1\\ j\neq i}}^{N} \prod\limits_{\substack{k=1\\ k\neq i\\ k\neq j}}^{N} (x_p - x_k)}{\prod\limits_{\substack{m=1\\ m\neq i}}^{N} (x_i - x_m)} \tag{30}$$

and N is the total number of points in the stencil. Similarly, for a second derivative at x_p

$$\left.\frac{\partial^2 f}{\partial x^2}\right|_{x_p} = \sum_{i=1}^{N} B_i f_i \tag{31}$$

where

$$B_i = \frac{\sum\limits_{\substack{\ell=1\\ \ell\neq i}}^{N} \sum\limits_{\substack{j=1\\ j\neq i\\ j\neq \ell}}^{N} \prod\limits_{\substack{k=1\\ k\neq i\\ k\neq j\\ k\neq \ell}}^{N} (x_p - x_k)}{\prod\limits_{\substack{m=1\\ m\neq i}}^{N} (x_i - x_m)}. \tag{32}$$

For the interior points a centered stencil is used thus requiring an odd number of points. An even number of points may be used but then the stencil is offset. For grid points near the boundary an offset stencil is used where the number of points in the stencil is maintained. It should be noted that the largest error from approximating the derivatives in this fashion will come from the second derivative approximation. To decrease this error more points can be used in the second derivative stencil than the first derivative stencil but here an equal number of points were used for each derivative approximation. These derivative operators are applied in physical space rather than computational space to avoid Runge's phenomena where spurious oscillations can occur for a one sided stencil with a high order of approximation. If the derivative operators of Eqs. (29) and (31) are applied to a centered stencil in computational space then the standard central finite difference coefficients are obtained. In other words, the fourth order method used by previous researchers can be obtained from the current method using a five point stencil in computational space.

There are a couple advantages to approximating the derivatives in this fashion. Once the subroutines for computing the coefficients are set up it is trivial to change the number of points used to approximate the derivatives. This makes it easy to switch from low to high order or *vice versa* without making any changes to the code as the order of the method is dependent upon the number of points chosen for the derivative stencils. Since the derivatives are taken in physical space rather than computational space grid metrics are not required. Although it is not used here, this allows an arbitrary placement of grid points within the computational domain. Also, the formulation for derivatives at the boundary can use the same derivative approximations which easily integrates high order boundary conditions into the code. As one of the main foci in the current work for developing a thermochemical nonequilibrium LST code was to include gas/surface interactions, wall normal derivatives are quite important making this technique a good fit.

After discretization, nonlinearities exist in α so the global method suggested by Malik[3] is used to compute the eigenvalue spectrum with $\alpha^2 = 0$. This method computes the eigenvalues from a generalized eigenvalue problem $\vec{A\phi} = \alpha\vec{B\phi}$ where the LAPACK[32] subroutine ZGGEV is used here for solution. From the eigenvalue spectrum an initial guess can be obtained for the local method which results in $\bar{A}\phi = \bar{B}$ and the eigenvalue is found iteratively without dropping the α^2 terms. The LAPACK subroutine ZGESV is used to solve the local problem. It is also possible to avoid the computationally intensive global method and obtain an initial guess for α from a nearby streamwise location, similar frequency, or a DNS simulation *assuming* the unsteady DNS results are available.

IV. Surface Chemistry Model and Boundary Conditions

For the two methods different boundary conditions are required. DNS boundary conditions are required at the wall, outlet, symmetry plane, and shock. For LST boundary conditions are required at the wall and outside the boundary layer or at the shock. Here LST boundary conditions are applied outside the boundary layer instead of at the shock.

A. DNS Surface Chemistry Model

The surface chemistry model accounts for reactions occurring at the graphite surface between the solid surface carbon and freestream gaseous species. Six surface reactions are taken into account: the first two reactions allow for surface removal of material through oxidation, the third reaction accounts for surface recombination of atomic oxygen, and the last three are due to sublimation of C, C_2, and C_3. C_3 is commonly included in most graphite ablation models as sublimation of graphite produces mostly C_3 with smaller amounts of C, C_2, and heavier carbon species.

The reactions and reaction probabilities for oxidation and recombination of atomic oxygen are obtained from Park[33] yielding

$$(\mathrm{C}) + \mathrm{O}_2 \rightarrow \mathrm{CO} + \mathrm{O} \tag{33}$$
$$(\mathrm{C}) + \mathrm{O} \rightarrow \mathrm{CO} \tag{34}$$
$$(\mathrm{C}) + \mathrm{O} + \mathrm{O} \rightarrow (\mathrm{C}) + \mathrm{O}_2. \tag{35}$$

The oxidation rates are based on kinetic theory giving

$$k_m = \alpha_m \sqrt{\frac{RT_w}{2\pi M_s}} \tag{36}$$

where α_m is the reaction probability for each reaction in Eqs. (33)–(35) respectively. The reaction probabilities are obtained experimentally yielding

$$\alpha_1 = \frac{1.43 \times 10^{-3} + 0.01 \exp\left(-1450/T_w\right)}{1 + 2 \times 10^{-4} \exp\left(13000/T_w\right)} \tag{37}$$
$$\alpha_2 = 0.63 \exp\left(-1160/T_w\right) \tag{38}$$
$$\alpha_3 = 0.63 \exp\left(-1160/T_w\right). \tag{39}$$

From which the associated surface species mass flux may be found from

$$\dot{m}_{O_2} = -\rho_{O_2} k_1 + \rho_O k_3 \tag{40}$$
$$\dot{m}_{CO} = \frac{M_{CO}}{M_{O_2}} \rho_{O_2} k_1 + \frac{M_{CO}}{M_O} \rho_O k_2 \tag{41}$$
$$\dot{m}_O = \frac{M_O}{M_{O_2}} \rho_{O_2} k_1 - \rho_O k_2 - \rho_O k_3. \tag{42}$$

There are three reactions for sublimation

$$(\mathrm{C}) \rightarrow \mathrm{C} \tag{43}$$
$$(\mathrm{C}) \rightarrow \mathrm{C}_2 \tag{44}$$
$$(\mathrm{C}) \rightarrow \mathrm{C}_3 \tag{45}$$

and for each reaction the mass flux is obtained from the Knudsen-Langmuir equation[34]

$$\dot{m}_s = \alpha_s \left(p_{v,s} - p_s\right) \sqrt{\frac{M_s}{2\pi R T_w}} \tag{46}$$

where α_s are experimentally determined[35] for each carbon species. The vapor pressure of the three carbon species is given by

$$p_{v,s} = \exp\left(\frac{P_s}{T_w} + Q_s\right) \quad p \text{ in atm} \tag{47}$$

where P_s and Q_s are from Ref. 18.

Boundary conditions are needed to couple the surface chemistry model with the gas model as well as set wall conditions for both temperatures and pressure. At the surface a surface energy balance is solved to find temperature and a surface mass balance is solved to find the mass fraction of each species. A simplified surface energy balance is used to avoid a complicated flow/solid coupling and allowing the focus of the simulation to stay on boundary layer stability. The surface energy balance is

$$k_T \frac{\partial T}{\partial n} + k_V \frac{\partial T_V}{\partial n} + \sum_{s=1}^{ns} \rho h_s D_s \frac{\partial c_s}{\partial n} = \sigma \epsilon T^4 + \dot{m} \sum_{s=1}^{ns} c_s h_{s,o} \tag{48}$$

where

$$h_{s,o} = \left(c_{v,s} + \frac{R}{M_s}\right) T + e_{v,s} + h_s^o + \frac{1}{2}\left(u_1^2 + u_2^2 + u_3^2\right) \tag{49}$$

and all values and derivatives are taken at the wall. $\epsilon = 0.9$ for the carbon surface and σ is the Stefan-Boltzmann constant. Each derivative is taken normal to the surface where n represents the direction normal to the surface. Derivatives of 5^{th} order Lagrange polynomials are used to compute the normal derivatives at the surface.

The surface mass balance for each species is

$$\rho_s u_n - \rho D_s \frac{\partial c_s}{\partial n} = \dot{m}_s. \tag{50}$$

where u_n is the wall normal velocity and each value or derivative is taken at the wall. The total mass balance found from summing Eq. (50) is

$$\rho u_n = \dot{m} \tag{51}$$

where the total mass flux is found from the sum of each species mass flux as

$$\dot{m} = \sum_{s=1}^{ns} \dot{m}_s. \tag{52}$$

For a wall with no velocity it is common to use pressure extrapolation or assume that $\frac{\partial p}{\partial n} = 0$ from the boundary layer assumptions. Here a finite wall velocity is obtained normal to the surface due to surface chemical reactions so it is also possible to use the one-dimensional subsonic inlet conditions. Instead, 5th order extrapolation is used which allows the high-order solution procedure for the interior points to set the wall pressure.

B. LST Boundary Conditions

As noted previously boundary conditions are required in the freestream and at the wall for LST. In the freestream, all perturbations are zero except the wall normal velocity perturbation which is found from the mass conservation equation similar to Stuckert.[36] At the wall the boundary conditions are slightly more complicated. There are $ns + 5$ independent variables in the stability calculations therefore $ns + 5$ conditions are required at the wall. Basically the approach taken here is to linearize all of the equations used to set the wall boundary conditions in the DNS simulation. Of these $ns + 5$ conditions the simplest are the no

slip in the wall tangent directions resulting in $\hat{u_1} = \hat{u_3} = 0$. The surface energy balance in Eq. (48) can be linearized resulting in

$$\frac{dT}{dy}k' + k\frac{\partial T'}{\partial y} + \frac{dT_V}{dy}k'_V + k_V\frac{\partial T'_V}{\partial y} + \rho\sum_{s=1}^{ns} h_s D_s \frac{\partial c'_s}{\partial y} + \rho\sum_{s=1}^{ns} h_s \frac{\partial c_s}{\partial y}D'_s + \rho\sum_{s=1}^{ns} D_s\frac{\partial c_s}{\partial y}h'_s + \left(\sum_{s=1}^{ns} h_s D_s \frac{\partial c_s}{\partial y}\right)\rho' - 4\sigma\epsilon T^3 T' - \dot{m}\sum_{s=1}^{ns} c_s h'_{s,o} - \dot{m}\sum_{s=1}^{ns} h_{s,o}c'_s - \left(\sum_{s=1}^{ns} c_s h_{s,o}\right)\dot{m}' = 0 \quad (53)$$

where the perturbation of the diffusion coefficients and the species mass flux terms are dependent on the specific gas model and surface chemistry model used. They can be found from a first order Taylor series expansion. Note that the overbars have been dropped from the steady terms for simplicity and y denotes the wall normal coordinate. As there are $ns+5$ independent variables it is required to put Eq. (53) in terms of these independent variables. Then the normal mode form for the perturbations may be substituted for the equation to be suitable as a boundary condition. For the gas model and surface chemistry model given here this results in

$$\begin{aligned}\frac{dT}{dy}\left(\sum_{r=1}^{ns}\frac{\partial k}{\partial \rho_r}\hat{\rho}_r + \frac{\partial k}{\partial T}\hat{T}\right) + k\frac{\partial \hat{T}}{\partial y} + \frac{dT_V}{dy}\left(\sum_{r=1}^{ns}\frac{\partial k_V}{\partial \rho_r}\hat{\rho}_r + \frac{\partial k_V}{\partial T}\hat{T} + \frac{\partial k_V}{\partial T_V}\hat{T}_V\right) + k_V\frac{\partial \hat{T}_V}{\partial y} \\ + \rho\sum_{s=1}^{ns} h_s D_s \frac{\partial}{\partial y}\left(\frac{\hat{\rho}_s}{\rho} - \frac{c_s}{\rho}\sum_{r=1}^{ns}\hat{\rho}_r\right) + \rho\sum_{s=1}^{ns} h_s\frac{\partial c_s}{\partial y}\left(\sum_{r=1}^{ns}\frac{\partial D_s}{\partial \rho_r}\hat{\rho}_r + \frac{\partial D_s}{\partial T}\hat{T}\right) \\ + \rho\sum_{s=1}^{ns} D_s\frac{\partial c_s}{\partial y}\left[\left(c_{v,s} + \frac{R}{M_s}\right)\hat{T} + \frac{\partial e_{v,s}}{\partial T_V}\hat{T}_V\right] + \left(\sum_{s=1}^{ns} h_s D_s\frac{\partial c_s}{\partial y}\right)\sum_{r=1}^{ns}\hat{\rho}_r - 4\sigma\epsilon T^3\hat{T} \\ - \dot{m}\sum_{s=1}^{ns} c_s\left[\left(c_{v,s} + \frac{R}{M_s}\right)\hat{T} + \frac{\partial e_{v,s}}{\partial T_V}\hat{T}_V + \frac{\dot{m}}{\rho}\hat{v}\right] - \frac{\dot{m}}{\rho}\sum_{s=1}^{ns} h_{s,o}\left(\hat{\rho}_s - c_s\sum_{r=1}^{ns}\hat{\rho}_r\right) \\ - \sum_{n=1}^{ns} c_n h_{n,o}\left[\sum_{r=1}^{ns}\sum_{s=1}^{ns}\frac{\partial \dot{m}_s}{\partial \rho_r}\hat{\rho}_r + \sum_{s=1}^{ns}\frac{\partial \dot{m}_s}{\partial T}\hat{T}\right] = 0 \quad (54)\end{aligned}$$

where all values and derivatives are found at the wall. To this point the derivation of the linearized surface energy balance has made no assumptions about parallel flow so it is still applicable to non-parallel methods. Recall from Eq. (51) that $\dot{m} = \rho u_2$ which requires any terms containing $\dot{m}$ to be set to zero to enforce the parallel flow assumption. Also, note that this equation is in essence imposing an upper bound on the temperature perturbation at the wall. Mack[2] notes that "for almost any frequency, it is not possible for the wall to do other than to remain at its mean temperature" which would require that $\hat{T} = 0$. In reality $\hat{T}$ at the surface may lie between these two extremes so it is useful to see how each boundary condition influences instabilities. Both of these cases are tested in Section VI. For either case of temperature perturbation the wall is assumed to be in thermal equilibrium resulting in $\hat{T}_V = \hat{T}$.

Conditions on each species density perturbation are required at the wall. Eq. (50) gives the condition on the species density at the wall for a DNS simulation. A linearization of this equation yields

$$\rho_s v' + \frac{\dot{m}}{\rho}\rho'_s - \rho D_s\frac{\partial}{\partial y}\left(\frac{\rho'_s}{\rho} - \frac{c_s}{\rho}\sum_{r=1}^{ns}\rho'_r\right) - \rho\frac{\partial c_s}{\partial y}D'_s - D_s\frac{\partial c_s}{\partial y}\sum_{r=1}^{ns}\rho'_r - \dot{m}'_s = 0 \quad (55)$$

where once again the overbars denoting steady conditions have been dropped for simplicity and $\dot{m}'_s$ is the species mass flux perturbation related to the specific gas/surface interaction model. Further linearizing the diffusion coefficient perturbation and species mass flux perturbation then substituting in the normal mode for each independent perturbation gives ns wall conditions in the form

$$\rho_s\hat{v} + \frac{\dot{m}}{\rho}\hat{\rho}_s - \rho D_s\frac{\partial}{\partial y}\left(\frac{\hat{\rho}_s}{\rho} - \frac{c_s}{\rho}\sum_{r=1}^{ns}\hat{\rho}_r\right) - \rho\frac{\partial c_s}{\partial y}\left(\sum_{r=1}^{ns}\frac{\partial D_s}{\partial \rho_r}\hat{\rho}_r + \frac{\partial D_s}{\partial T}\hat{T}\right) - D_s\frac{\partial c_s}{\partial y}\sum_{r=1}^{ns}\hat{\rho}_r - \sum_{r=1}^{ns}\frac{\partial \dot{m}_s}{\partial \rho_r}\hat{\rho}_r - \frac{\partial \dot{m}_s}{\partial T}\hat{T} = 0. \quad (56)$$

Once again note that the parallel flow assumption has not been made yet. To make the parallel flow assumption simply drop the terms with $\dot{m}$. Note that the equation can be further simplified if $\hat{T} = 0$ by dropping all $\hat{T}$ terms.

With the species surface mass balance linearized recall that a total mass balance was used to set the wall normal velocity (Eq. (51)) in the DNS simulation. Further recall that this condition is found from a linear combination for each species surface mass balance therefore a linearization of this equation will result in no new information at the boundary. For the boundary to be adequately constrained another equation is required. In the DNS simulation pressure extrapolation is used to account for the incoming characteristic at the wall. Linearizing the pressure extrapolation condition accounts for the last required boundary condition and is used in place of a $\hat{v}$ equation. It is also possible to linearize the total mass flux equation and substitute the linearized pressure extrapolation condition for one of the linearized surface mass balance equations. Both methods were tested and the differences between the two were negligible.

V. LST Validation

To validate the LST code with the full linearized ablation boundary conditions a comparison is performed between the results of the LST code and results from a DNS simulation. In the DNS simulation the entire flow field is computed with a disturbance imposed in the freestream which differs from LST where only a single wall normal slice is required and no disturbance is introduced. Some of the simplifying assumptions made in the derivation of the LST equations are not made in DNS such as the parallel flow assumption but both methods for this case do assume that disturbances are linear. Achieving an accurate comparison between the stability results of these two different stability methods will lend credibility to the proper implementation of both methods.

A. Grid Convergence Study

Before a code comparison can be performed a grid convergence study must be done to determine the required number of grid points for the LST grid. Three different grid densities were used with 100, 200 and 300 points respectively. A comparison for the amplification rate at multiple frequencies as well as the temperature perturbation amplitude for a 525 kHz disturbance is given in Figure 1. For the 200 grid point solution the percent relative error for the amplification rate is less than one percent for the majority of the unstable frequency range. The error increases near the edges of the frequency range because the amplification rate is near zero. There are only slight changes in the temperature perturbation amplitude between all three solutions. Two hundred grid points yields a grid converged solution for this streamwise location.

B. LST Comparison to DNS

In the DNS simulation fast acoustic waves in the freestream are imposed on the bow shock and then their behavior is simulated as they pass through the entire domain. This approach does not simulate the behavior of a single mode like LST but rather multiple modes can be present for each frequency. For the most consistent comparison a streamwise location was selected where DNS results showed a constant exponential disturbance growth. This was done because constant exponential growth is indicative of modal growth and therefore a dominant boundary layer mode rather than multiple competing modes. The streamwise location selected is located at s=0.564 m downstream measured along the cone surface from the stagnation point.

Figure 2 shows the steady boundary layer profile computed by DNS. Here u and v represent the velocity components parallel to the wall and normal to the wall respectively. Significant thermal nonequilibrium is present in the boundary layer even though the wall boundary conditions for the simulation puts the two temperatures into thermal equilibrium. The no-slip condition is present for the u velocity component and wall normal blowing is less than 1 m/s. The only significant carbon species in the boundary layer is CO which has a mass fraction of 0.123 at the wall and decreases quickly away from the wall. The temperatures are high enough for dissociation of oxygen to occur but not high enough for nitrogen to dissociate significantly.

Figure 3 gives a comparison of the perturbation amplitude for a second mode disturbance ($\beta = 0$) of translation-rotation temperature, vibration temperature, pressure, and densities of N_2, O_2, CO, N, O, and C. For both temperatures the comparison is quite good. Both the tempertaure and its gradient near the wall compares well. The linearized surface energy equation which is used in conjunction with the other boundary conditions to set the translation-rotation temperature at the wall accurately compares with the DNS results.

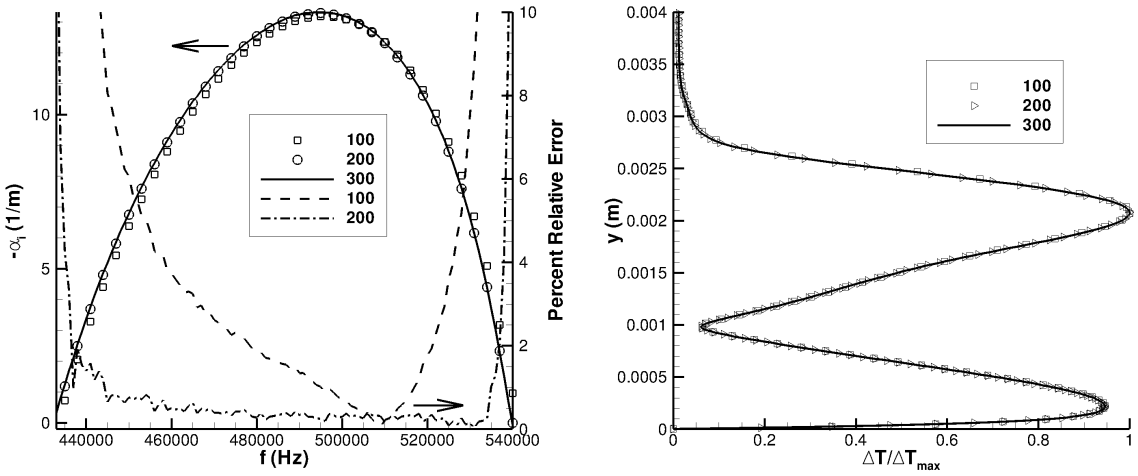

(a) (b)

Figure 1. Comparison of (a) amplification rate and (b) temperature perturbation amplitude for three different grid densities.

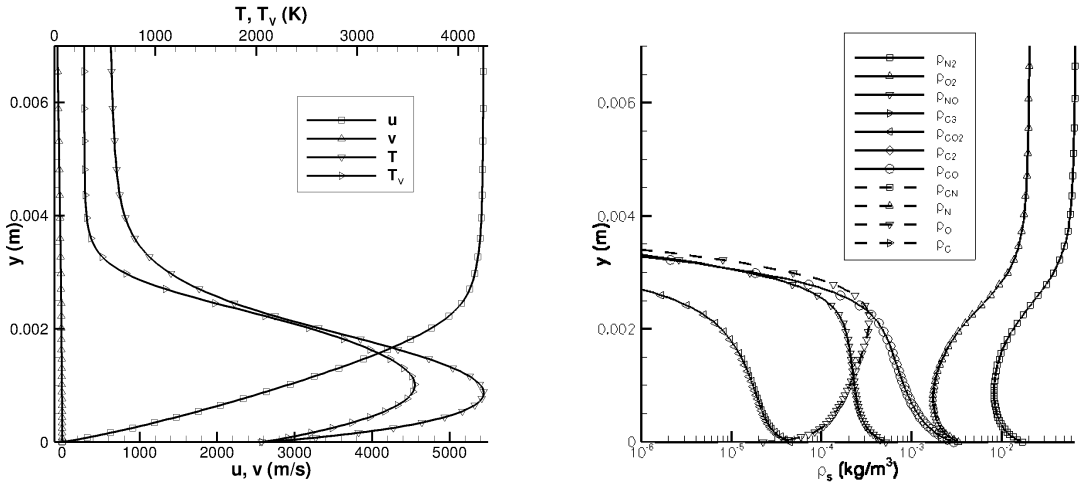

(a) (b)

Figure 2. Boundary layer profiles at s=0.564 m for (a) velocity and temperature, and (b) species density.

Similarly, each density perturbation and its near wall gradient compares well with the DNS results near the wall showing that the linearized surface mass balances are implemented correctly. The pressure perturbation which is a combination of each density perturbation and the translation-rotation temperature also compares well.

It is also possible to compare the growth rate and wavenumber i.e. the real and imaginary parts of alpha obtained from LST to a DNS simulation. It is difficult to make a comparison at a single location so multiple streamwise locations are used. Figure 4(a) shows the wavenumber comparison for a 525 kHz second mode disturbance where s is the streamwise distance measured from the stagnation point. The wavenumber computed from LST compares well with the DNS simulation. Upstream near $s = 0.2$ m the 525 kHz is just becoming unstable in the DNS simulation so the second mode is not dominant yet. Moving downstream the second mode starts to become dominant as witnessed by the lessening fluctuations and the comparison between the two is much better. A similar trend is seen in Figure 4(b) where a comparison of the growth rate

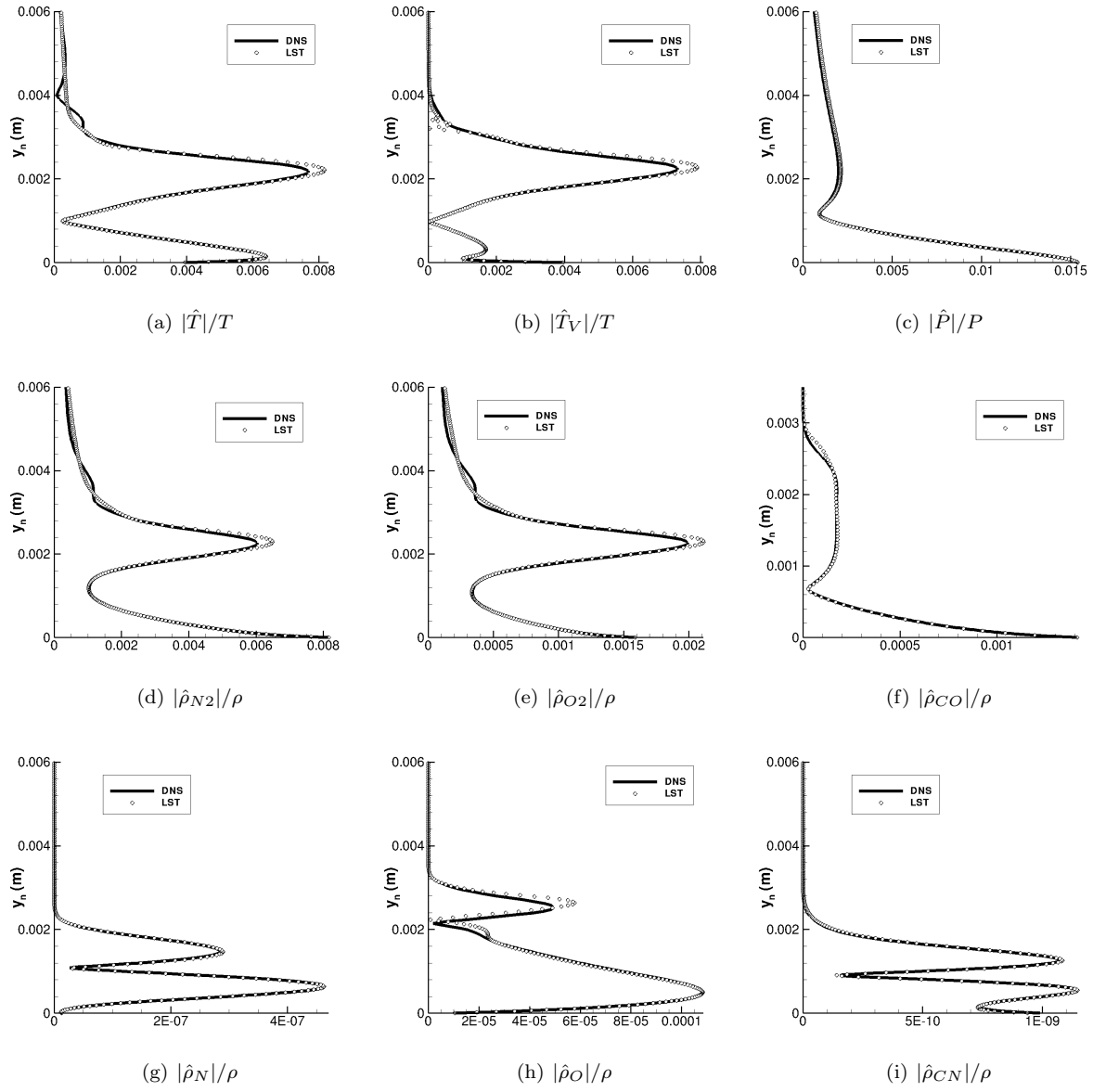

(a) $|\hat{T}|/T$ (b) $|\hat{T}_V|/T$ (c) $|\hat{P}|/P$

(d) $|\hat{\rho}_{N2}|/\rho$ (e) $|\hat{\rho}_{O2}|/\rho$ (f) $|\hat{\rho}_{CO}|/\rho$

(g) $|\hat{\rho}_N|/\rho$ (h) $|\hat{\rho}_O|/\rho$ (i) $|\hat{\rho}_{CN}|/\rho$

Figure 3. Eigenfunction amplitude comparison for a 525 kHz second mode disturbance between DNS and LST at s=0.564 m for select variables.

is given. Upstream there are large fluctuations in growth rate that damp downstream. The growth rate from the LST code seems to be in general higher than the DNS results. This is to be expected as including the curvature terms in LST is stabilizing to the second mode. Therefore, including the curvature terms would decrease the growth rate to compare better with the DNS results.

C. Order of Error Estimate

As the derivative operators used to solve Eq. (25) are implemented in a non-standard fashion an order of error estimate is given to show the approximate order of the error incurred. An error estimate can be obtained using three different doubled grids using

$$2^p \approx \frac{||S_{h/2} - S_h||_2}{||S_{h/4} - S_{h/2}||_2} \tag{57}$$

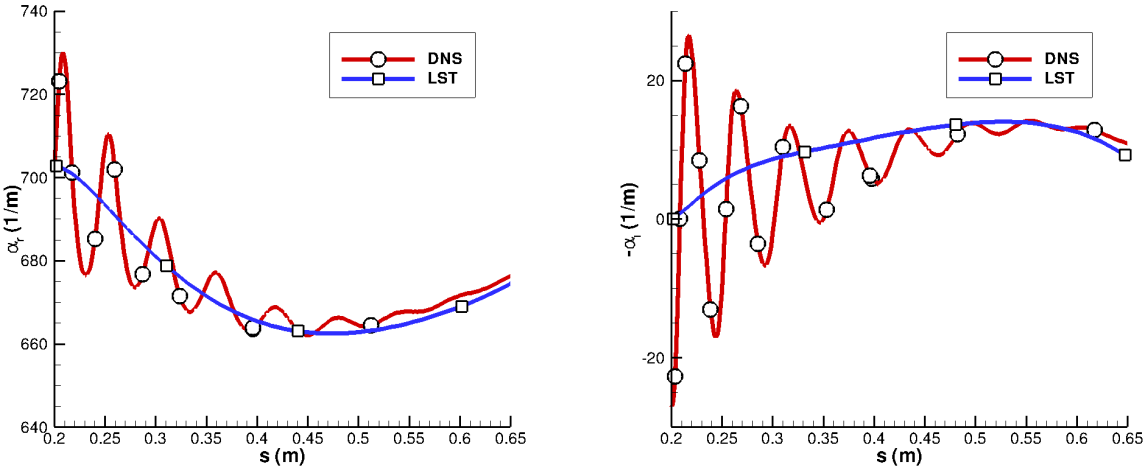

(a) (b)

Figure 4. LST comparison to DNS for the (a) wavenumber and (b) growth rate of a 525 kHz second mode disturbance.

where p is the approximate order of the error, S is the solution at the different grid densities, and h denotes the grid spacing. The norm used here is the 2-norm. A test was run using a five point stencil for all grid points and the derivative approximations in physical space of Eqs. (29) and (31). Three grid densities were used: 101 points, 201 points and 401 points where the 2-norm was computed for each point in the 101 point grid. This resulted in $p = 3.91$ which denotes a fourth order method.

In the previous research of Ref. 14 a fourth order central approximation was used for interior derivatives, a second order central approximation was used one point away from the boundary and a first order approximation was used at the boundaries. Each of these was taken using the standard centered finite difference stencil in computational space similar to Ref. 7. The same method for estimating the order of the error was repeated. This resulted in $p = 1.86$ which denotes a second order method. Clearly the method using a consistently five point stencil rather than switching to first order on the boundaries gives the method with the highest rate of convergence. It was for this reason that the method given here was updated from Ref. 14.

VI. Linear Stability Analysis of $M_\infty = 15.99$ Blunt Cone

LST is able to predict instability waves and their corresponding growth rates from steady boundary layer profiles. The characteristics of the instability wave are strongly tied to the meanflow boundary layer profile which is taken as an input to the LST code. It is possible to use a single meanflow boundary layer profile computed using one gas model and then change gas models in an LST code to predict how the characteristics of *only* instability waves will behave with changing models. This has been done to good effect by previous researchers.[8] Since instability waves are tied so strongly to the meanflow profiles, to predict how different gas types i.e. ideal gas and real gas effect the entire process of hypersonic boundary layer stability the meanflow as well as the computation of instability waves needs to be performed with each of the separate models. Similarly, both a meanflow and instability waves need to be computed to assess the overall effect of surface chemistry such as wall catalycity and surface ablation on hypersonic boundary layer stability. By computing a meanflow and the corresponding instability waves with the different models an accurate comparison of the gas effects on stability, rather than simply the instability waves, can be given.

A. Steady State Solutions of $M_\infty = 15.99$ Blunt Cone

In this research one of the goals is to assess real gas effects and surface ablation effects, which are in the form of surface chemistry, on hypersonic boundary layer stability. To do this five distinct steady simulations were run. Each of these steady simulations has the same geometry and the same freestream conditions. The

geometry for each case is a sphere cone with a nose radius of 0.00635 m and a cone half angle of 7°. The freestream conditions are listed in Table 1. The cone axis is aligned with the freestream flow yielding an angle of attack equal to zero. The freestream unit Reynolds number and stagnation enthalpy are $Re_u = 7.3 \times 10^6$ /m and $h_{o,\infty} = 15.3$ MJ/kg respectively. This is a high enthalpy case where thermochemical nonequilibrium effects are significant and still present well downstream of the nose.

Table 1. Freestream conditions.

M_∞	15.99
ρ_∞	2.4093×10^{-2} kg/m^3
P_∞	2026.0 N/m^2
$c_{N_2,\infty}$	0.7635
$c_{O_2,\infty}$	0.2365

Each of the five meanflow cases are listed in Table 2. Case 1a and 1b have the same meanflow profile which is computed by the eleven species thermochemical nonequilibrium model with ablation boundary conditions. The surface temperature profile computed from Case 1 is used to set the wall temperature for Cases 2–5. Case 2 is a five species air thermochemical nonequilibrium simulation with surface blowing. The five species air gas model is the exact same as the N_2, O_2, NO, N, O components in the eleven species model. The imposed surface blowing has the same mass flux as Case 1 but standard freestream air is blown instead of carbon products. Case 3 is the same as Case 2 except there is no blowing at the surface. Also, the surface recombination of atomic oxygen (Eq. (35)) is retained for both Cases 2 and 3. Cases 4 and 5 are both ideal gas cases which use the same nonequilibrium code with the source terms turned off, the vibration energy held constant, and the mass fractions held to their freestream values. This is done so the viscosity, thermal conductivity, etc. are calculated the exact same way for each of the five meanflow cases. Case 4 has the same mass flux profile as Case 1 and Case 2 while Case 5 has no blowing.

Table 2. Types of steady simulations.

Case Number	Type	Number of Species	Blowing	LST BCs
1a	Real Gas	11	Ablation	full linearized ablation
1b	Real Gas	11	Ablation	$\hat{T}_w = 0$
2	Real Gas	5	Yes	
3	Real Gas	5	No	
4	Ideal Gas	2	Yes	
5	Ideal Gas	2	No	

Before moving further the LST wall boundary conditions for each of these cases needs to be covered briefly. The difference between Cases 1a and 1b is the boundary conditions used in the stability computations. In Case 1a the full linearized ablation model is used while in Case 1b the linearized surface energy balance (Eq. (54)) is replaced with $\hat{T}_w = 0$. For Cases 2–5 $\hat{T}_w = 0$ as the wall meanflow temperature is set from Case 1. For Cases 2 and 3 the corresponding surface mass balances are linearized to provide conditions for species perturbations at the wall. Note that this is the same as described previously in Section B but the mass flux terms where carbon species are produced are dropped. For Cases 4 and 5 the fluctuation of the composition is forced to zero i.e. $c_s' = 0$.

Note that the same LST code was used for each of the cases. For Cases 2 and 3 only changes to the boundary conditions were required. For Cases 4 and 5 all species and their perturbations except N_2 and O_2 were forced to zero, the meanflow as well as the perturbation vibration temperature was forced to zero, source terms and their derivatives were forced to zero, and k_V and D_s with their derivatives were forced to zero. Also, the boundary conditions for Cases 4 and 5 were changed.

For each meanflow case the wall temperature is the same i.e. the wall temperature computed from Case 1 is used to set all other cases. The wall temperature is shown in Fig. 5(a). Note that there is a strong decrease in the wall temperature starting from the cone nose ($s = 0$) and continuing downstream. This is

common in ablative flows as the highest wall temperature is commonly at the stagnation point and then decreases downstream until the onset of turbulence. There is no onset of turbulence here hence no marked increase in wall temperature. This decrease in temperature has a strong impact on boundary layer height. Figure 5(b) shows the height of the boundary layer for a portion of the cone frustum. Notice that the boundary layer is decreasing in the downstream direction rather than increasing. At first this may seem counterintuitive as generally the boundary layer is increasing in the downstream direction. In this case the strong decrease in wall temperature cools the boundary layer which contracts the flow and the height of the boundary layer decreases. It has been shown in previous experimental research that the height of the boundary layer is nearly half the wavelength of the dominant second mode disturbance.[37] The phase velocity of the dominant second mode can be roughly approximated as the boundary layer edge velocity leading to $c_r \approx const. \approx \omega/\alpha_r \approx 2\omega h$. Meaning as h decreases ω increases. With this piece of information one would expect to find that the unstable frequency range for the ideal gas case would move downstream. Precisely this will be shown from a linear stability analysis.

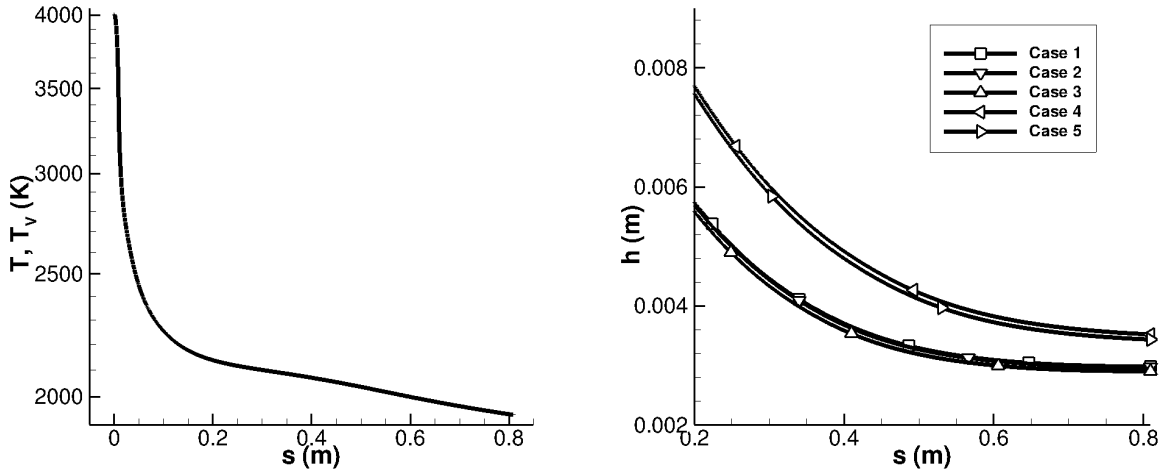

(a) (b)

Figure 5. Meanflow (a) wall temperature and (b) velocity boundary layer thickness.

Before moving on to a linear stability analysis a comparison of all five meanflow profiles is given for a single streamwise location ($s = 0.564$ m) in Fig. 6. In Ref. 14 the results of a grid convergence study are given showing that the proper grid is used for the meanflows. There is only a small difference in the streamwise velocity profiles. The height of the velocity boundary is larger for cases 4 and 5 which is to be expected as cases 4 and 5 are perfect gas. Similarly, the height of the temperature boundary layer is larger for the perfect gas cases. It is also possible to compare the species densities between all five cases noting that for perfect gas $\rho_{N2} = c_{N2,\infty}\rho$. As the temperature in the boundary layer is not high enough for N_2 to significantly dissociate or react with other species ρ_{N2} is nearly the same for Cases 1–3. However, there is a difference in the density of oxygen. In Case 1 ablation has introduced carbon products into the flow and this far downstream most of the carbon is in the form of CO. This means that for each carbon atom in CO an oxygen atom is needed which will reduce the density of oxygen for Case 1. This behavior is not seen in Case 2 or 3 as there are no carbon species.

B. Instability Characteristics of $M_\infty = 15.99$ Blunt Cone

LST gives information about what disturbance frequencies are unstable and the corresponding growth rates of those frequencies but there is no information on the amplitude of the incoming disturbance. To estimate boundary layer transition using LST the e^N transition criterion is used which is defined as

$$e^N = \frac{A}{A_0} = \exp\left(-\int_{s_0}^{s} \alpha_i dx\right). \tag{58}$$

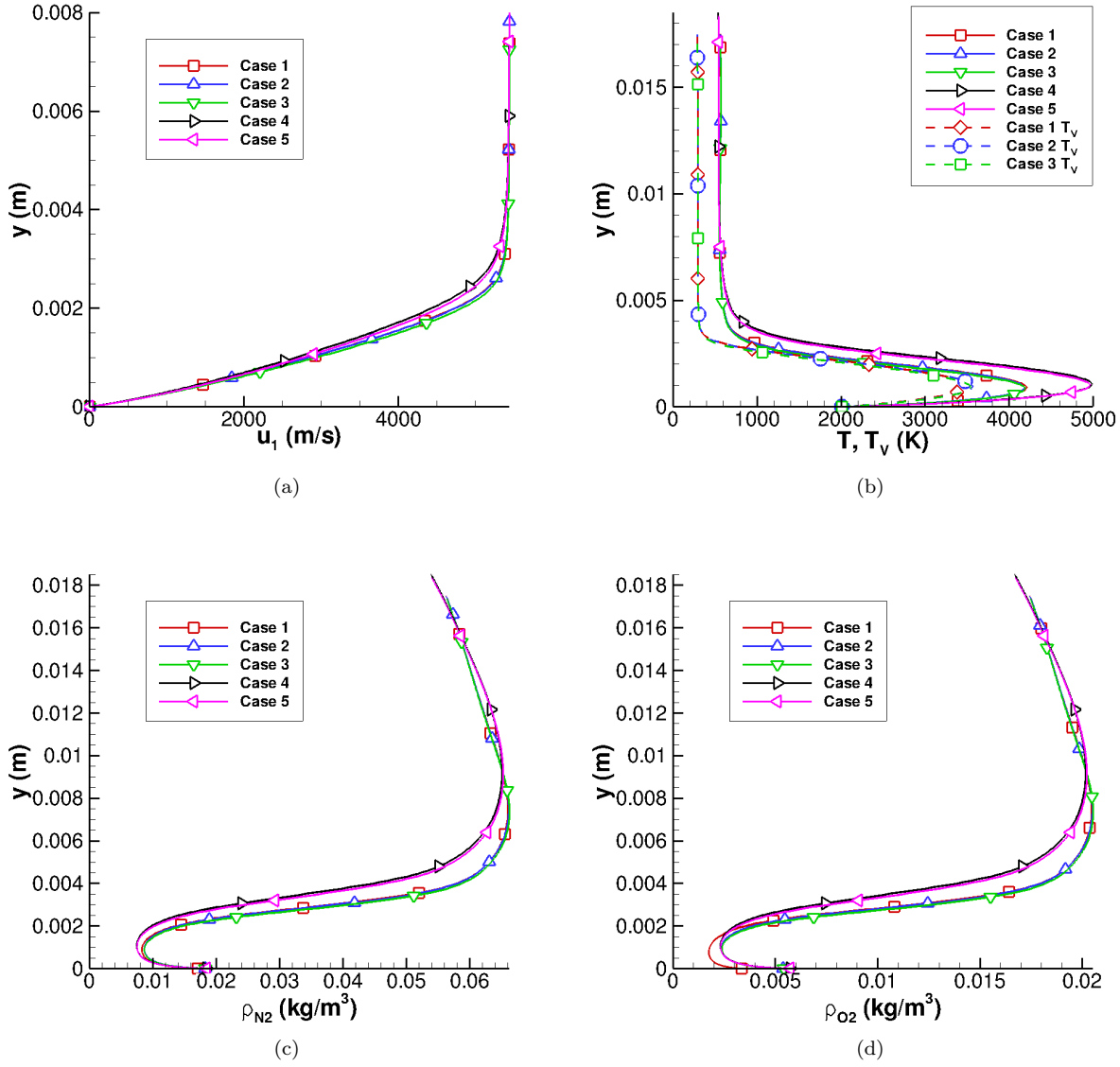

Figure 6. Meanflow profile comparison at s=0.4 m.

Here A is the integrated disturbance amplitude, A_0 is the initial amplitude, s_0 is the location where the disturbance first becomes unstable and α_i is the spatial amplification rate. The integration is performed for a constant frequency ω. Note that a negative imaginary part of the wavenumber α results in disturbance growth while a positive value results in disturbance decay. The N factor is specifically the exponent of e^N. In flight transition N factors are commonly understood to be around 10 while in ground test facilities the N factor is usually lower.

Before creating an N factor plot it is required to locate the second mode before tracing it either downstream or upstream. To aid in locating the second mode for various frequencies a plot of the fast and slow modes is obtained at a single streamwise location ($s = 0.564$ m). Figure 7 shows the phase velocities, wavenumbers, and growth rates for the fast and slow modes for Case 4. The fast mode appears near $c_r = 1 + 1/M_\infty = 1.063$ and the slow mode appears near $c_r = 1 - 1/M_\infty = 0.937$. The slow mode is the mode that turns into the second mode as the frequency increases. This can be seen as α_i becomes negative for the slow mode indicating disturbance growth. A similar analysis is performed for Case 1b and is shown in Fig. 8. Similarly, the slow mode becomes the second mode as witnessed by the growth rate ($-\alpha_i$). Note that for both Case 1b and Case 4 that there are no unstable first mode disturbances.

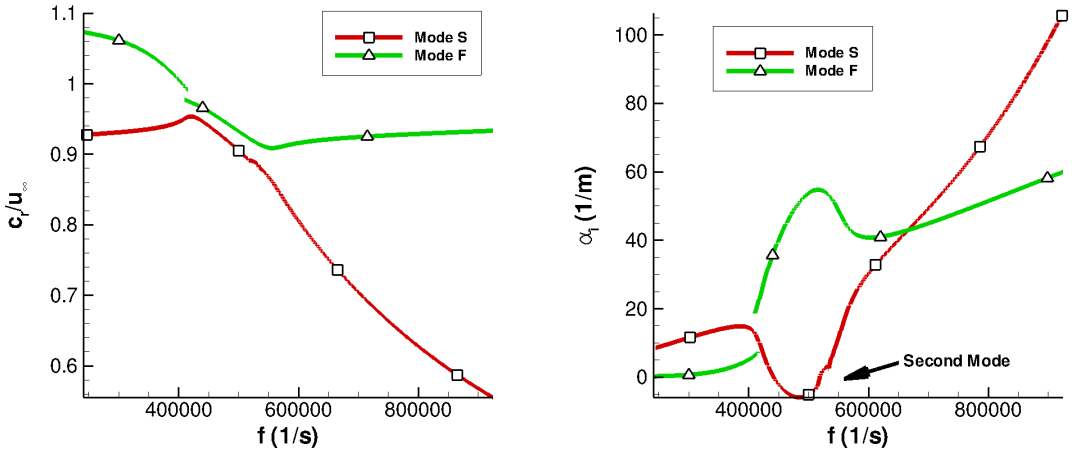

(a) (b)

Figure 7. Case 4 fast and slow mode plot of (a) phase velocity and (b) α_i or the negative growth rate.

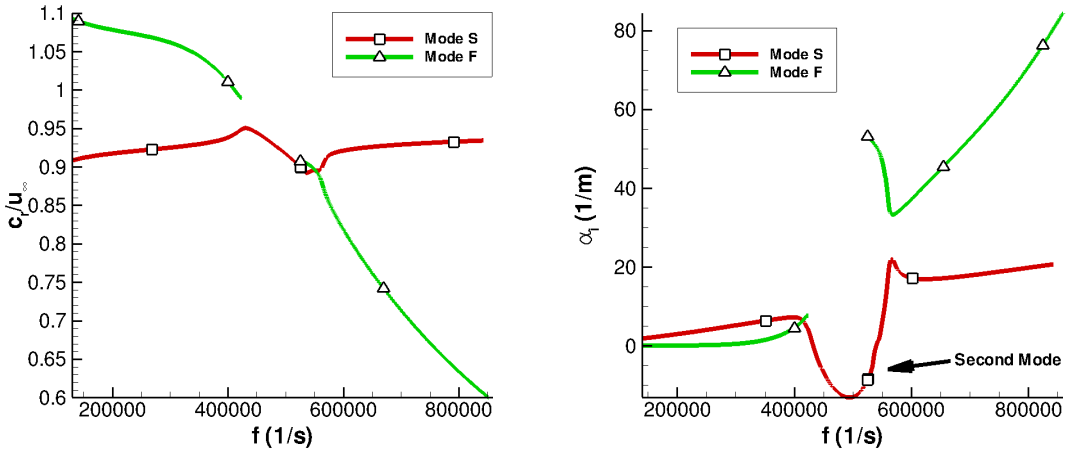

(a) (b)

Figure 8. Case 1b fast and slow mode plot of (a) phase velocity and (b) α_i or the negative growth rate.

Before analyzing boundary layer instabilities it is useful to visualize what is happening in the boundary layer as unstable disturbances are growing. Fig. 9 shows an oxygen density disturbance representative of initial second mode growth. Initially the disturbances in the boundary layer are the same order of magnitude as other disturbances originally introduced in the freestream. Moving downstream the boundary layer disturbances will grow exponentially (Fig. 10) and dominant any incoming disturbance. Also note the cyclic behavior of the boundary layer disturbances. This behavior is assumed during the derivation of the linear stability theory equations (Eq. (25)).

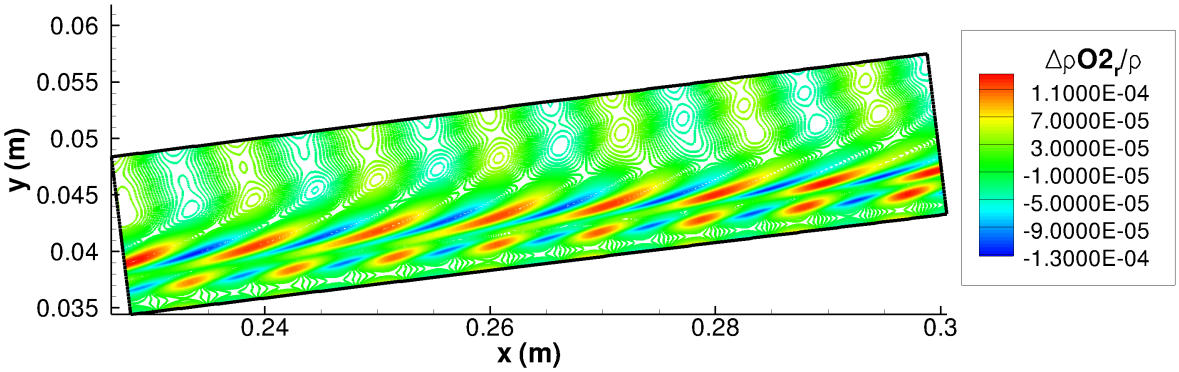

(a)

Figure 9. Case 1a instantaneous perturbation contour plot of oxygen for a 525 kHz frequency disturbance.[14]

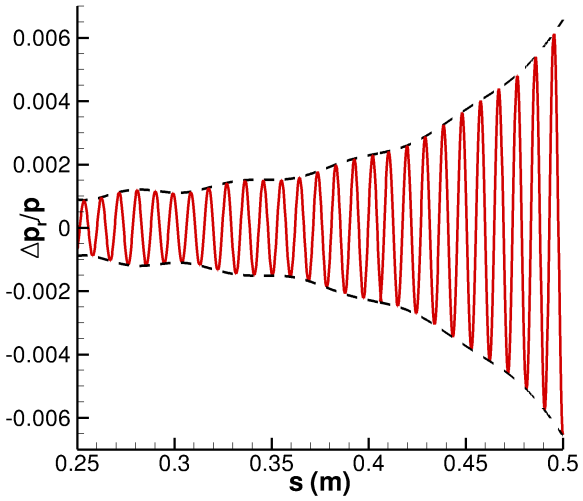

(a)

Figure 10. Case 1a exponential growth of wall pressure perturbation.

Now that the second mode is known it is possible to trace it upstream and downstream to find the second mode N factor. There was no attempt to vary the wave angle from $\beta = 0$ to find the most unstable first mode disturbances. For a high Mach boundary layer flow the first mode has a much less pronounced effect on boundary layer stability therefore its effects can be safely ignored when computing the N factor. Figure 11 shows the N factor plots for each of the six cases. The case with the largest N factor is Case 1a where the N factor is 6.8 at the exit of the domain. This means that from the neutral point the disturbance has grown 898 times or approximately three orders of magnitude. The corresponding frequency for this maximum N factor of Case 1a is 500 kHz. The second largest N factor is found from Case 1b where N=5.2

and the corresponding frequency is 487.5 kHz. Recall that the only difference between Cases 1a and 1b is the temperature perturbation boundary condition which is $\hat{T}_w = 0$ for Case 1b. Assuming that the amplitude at the neutral point is the same for both cases then $e^{7.8}/e^{5.2} = A_{1a}/A_{1b} = 13.5$. This shows that the largest amplitude for Case 1a is roughly one order of magnitude larger than the largest amplitude disturbance for Case 1b. Also, the frequency is shifted to a slightly lower frequency for Case 1b. Clearly there is a large difference in the boundary layer's stability due to the different boundary conditions for the wall temperature perturbation.

From Figs. 11(b) and 11(c) it is possible to note the differences that result due to changing the wall blowing from ablation to blowing air at the freestream mass concentration. Essentially this would be measuring the effect of carbon species due to ablation in the boundary layer as opposed to only five species air in the boundary layer. For Case 1a the largest N factor is 5.2 at 487.5 kHz. In Case 3 the maximum N factor is 4.8 at a frequency of 487.5 kHz. This results in a difference of one and a half times which shows that carbon species slightly destabilize the boundary layer but the difference is small. Also, the frequency for the two cases remains the same. It should be noted that as blowing increases there will be more mass from carbon species in the boundary layer. Assuming that the same trend is followed this will more strongly destabilize the boundary layer. Also, if the estimated ablation rates are low it would be possible to predict transition in a second mode dominated graphite ablative flow by assuming the surface blowing to be composed of air rather than various carbon products.

It is also possible to isolate the effects of blowing on real gas hypersonic boundary layer stability. Figs 11(c) and 11(d) show Case 2 and 3 where Case 2 has blowing and Case 3 does not. The largest N factor for Case 2 is 5.2 at 487.5 kHz. The largest N factor for Case 3 is 4.4 at 500 kHz which results in an amplitude change of 2.2 times. This shows that the boundary layer with blowing is destabilized compared to the boundary layer with no blowing. Note that the blowing profile is large upstream near the nose but small downstream of the nose. Similarly, blowing effects on an ideal gas hypersonic boundary layer can be seen by comparing Figs. 11(e) and 11(f). The maximum N factor for Case 4 is 2.02 and the maximum N factor for Case 5 is 1.98. The difference between these two cases is minute showing that for the ideal gas boundary layer blowing has a negligible effect on boundary layer stability in this particular case.

Finally it is possible to analyze real gas effects by comparing Case 2 with Case 4 and Case 3 with Case 5 (Figs 11(c) and 11(e) and Figs 11(d) and 11(f) respectively). The difference in maximum N factor between Cases 2 and 4 is 2.6 which results in a disturbance that is 13.5 times larger for Case 2. This is a significant difference. Here, real gas causes the largest disturbance to grow an order of magnitude more than the ideal gas case. Note also that the unstable frequency range has moved downstream for the ideal gas case. This is to be expected as the height of the boundary layer is decreasing in the downstream direction (recall Fig. 5(b)). Similar results are seen by comparing Cases 3 and 5. The difference in maximum N factor is 2.4 which gives a disturbance amplitude 11 times larger for Case 3. Also, the unstable frequency range has again shifted downstream. Therefore, in this particular case, real gas effects are destabilizing to the hypersonic boundary layer. Real gas effects in both comparisons result in a maximum disturbance at the domain exit that is one order of magnitude larger than for the corresponding ideal gas case.

As seen in Eq. (58) the N factor is obtained by integrating the growth rate in the streamwise direction. By examining the growth rates corresponding with each N factor it can be seen exactly how the growth rate is influencing the N factor. A growth rate plot for each case is given in Fig. 12. Comparing Cases 1a and 1b the growth rate for each frequency is overall slightly larger for Case 1a. Also, the range along the cone for the unstable frequencies is larger for Case 1a i.e. a frequency for Case 1a is unstable over a larger length of cone. Noting these differences the large change in N factor between Cases 1a and 1b is most likely due to the larger range over which the frequencies are unstable.

Comparing Cases 1b and 2 the growth rate for Case 1b is larger than Case 2 while the unstable range for both cases is almost the same. As the difference between these cases is the carbon species this means that the carbon species are the cause of the increased amplification rate of second mode disturbances. Most likely the difference in N factor between Cases 1b and 2 can be explained by the larger growth rate seen by Case 1b. Comparing Cases 2 and 3 it can be seen that the growth rate is nearly the same for both cases therefore the difference in N factor must be explained by a larger unstable range for Case 2. Here blowing is causing the unstable region to become larger for the most unstable frequencies in the domain. Note the difference between the effects of carbon species and blowing on real gas second mode instability. Carbon effects increase the growth rate while blowing is not increasing the growth rates but rather increasing the length over the cone that the frequencies are unstable.

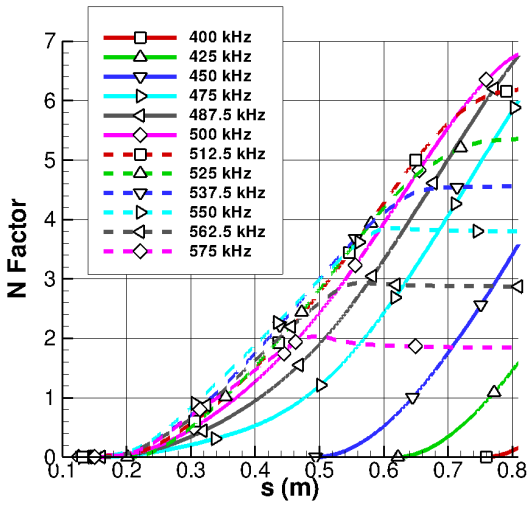

(a) Case 1a

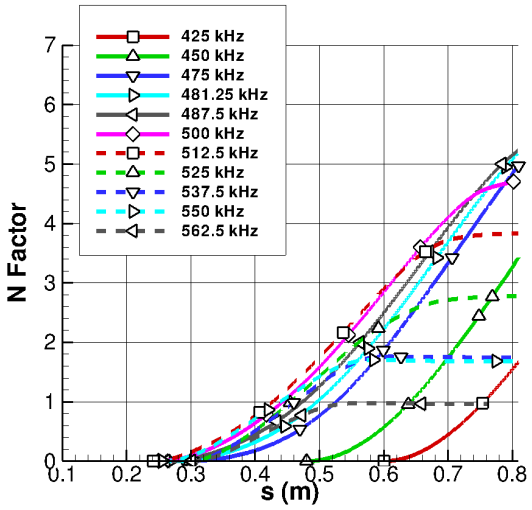

(b) Case 1b

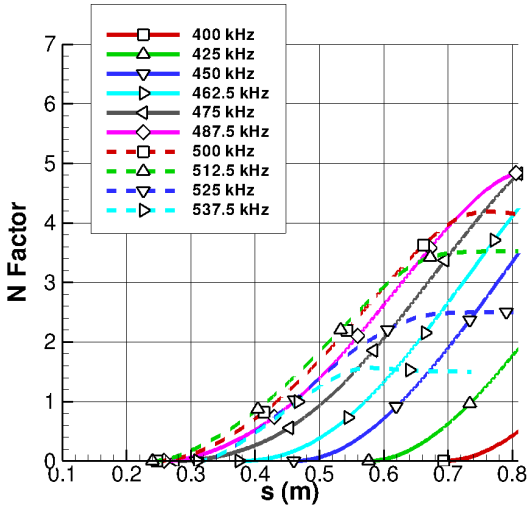

(c) Case 2

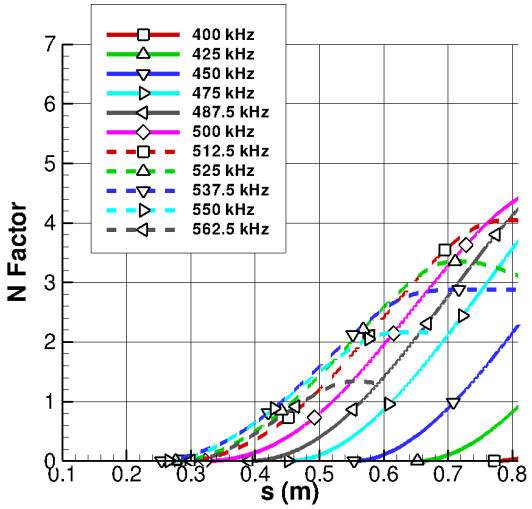

(d) Case 3

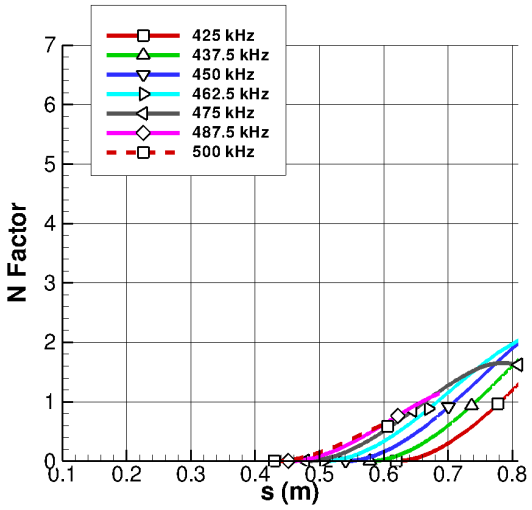

(e) Case 4

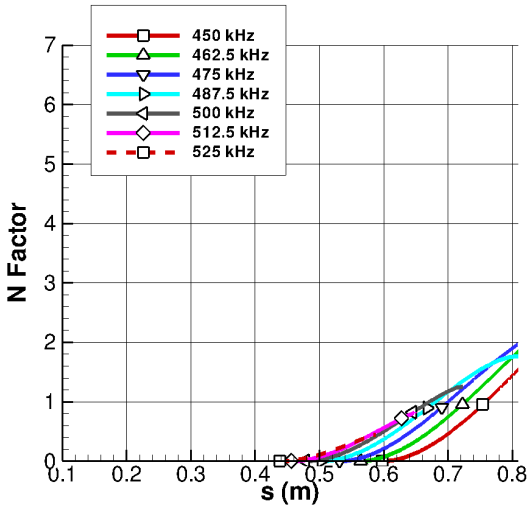

(f) Case 5

Figure 11. N factor comparison.

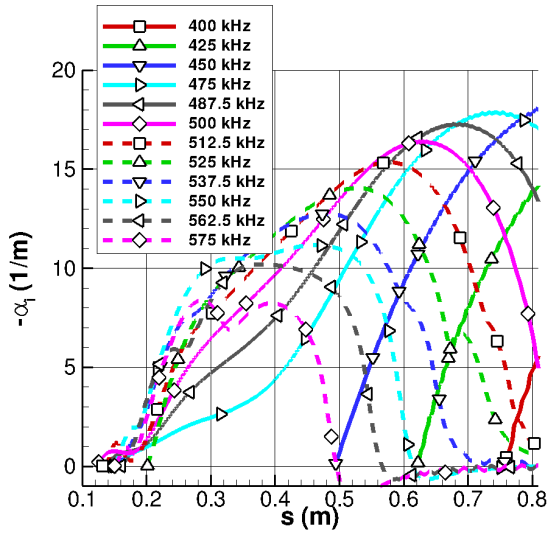

(a) Case 1a

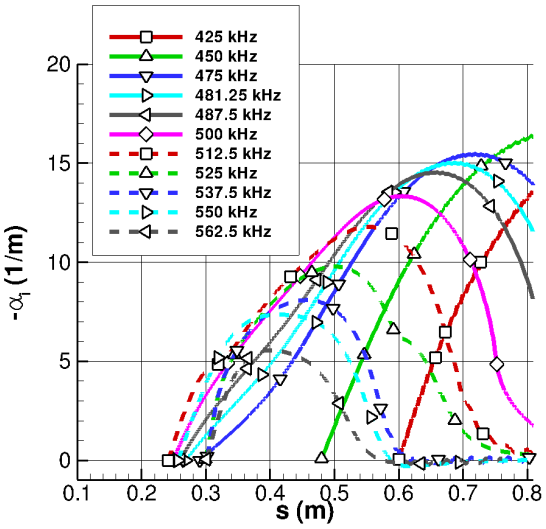

(b) Case 1b

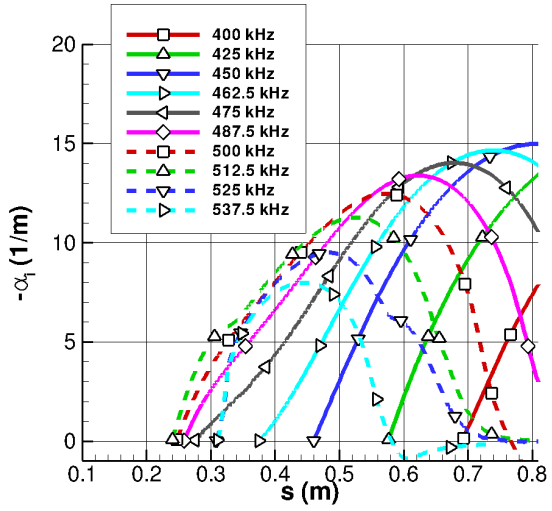

(c) Case 2

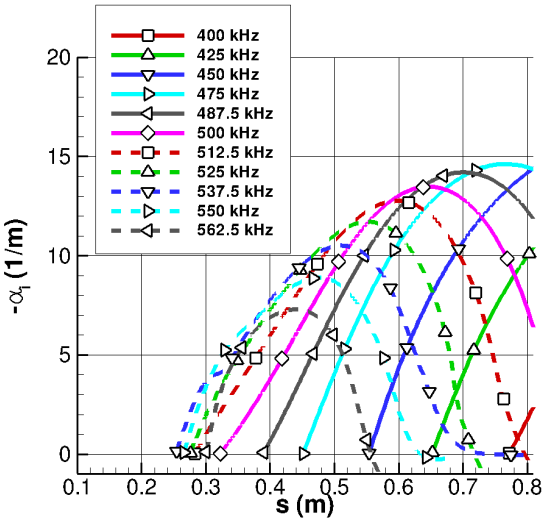

(d) Case 3

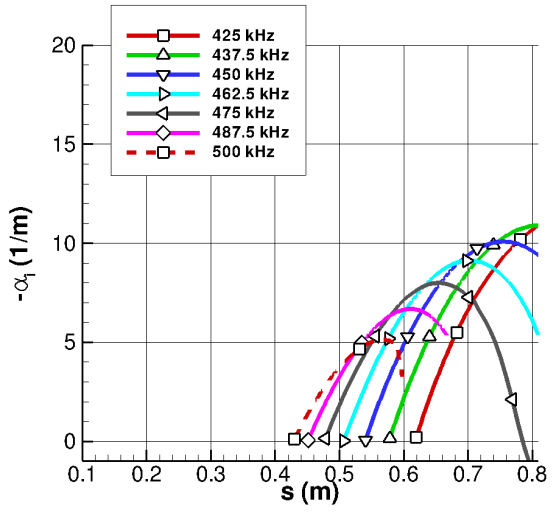

(e) Case 4

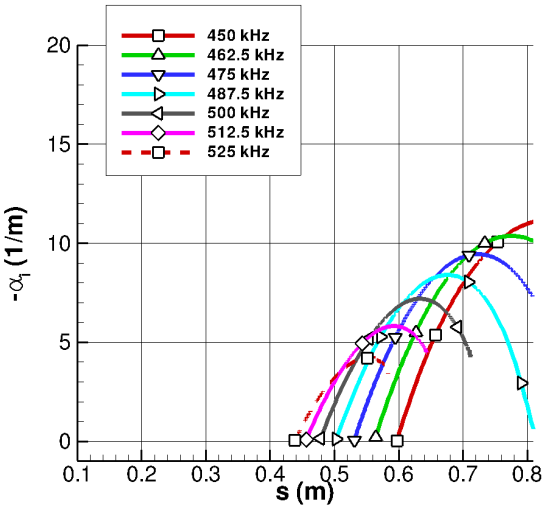

(f) Case 5

Figure 12. Growth rate ($-\alpha_i$) comparison.

When closely examining the growth rates of Cases 1a, 1b, 2, and 3 one may notice that the highest frequency is not always the first unstable frequency. For example, notice Fig. 12(c) where the highest frequency included in the calculations is 537.5 kHz and it crosses from stable to unstable near $s = 0.31$ m. Looking upstream of $s = 0.31$ m one can see that there are lower frequencies than 537.5 kHz that are already unstable. This behavior is most likely due to the rapidly decreasing boundary layer thickness causing some higher frequencies to become unstable later. This behavior is not seen for either Case 4 or Case 5 as there are no significant second mode instabilities when the boundary layer is strongly decreasing. This raises the question of the validity of LST in regions where there is a relatively rapid decrease in boundary layer height. Further DNS research is underway to compare with and hopefully validate the results obtained from LST.

Once again it is possible to analyze real gas effects by comparing Case 2 with Case 4 and Case 3 with Case 5 (Figs 12(c) and 12(e) and Figs 12(d) and 12(f) respectively). Comparing Cases 2 and 4 it can be seen that the growth rates for the real gas are larger than for the ideal gas. Also, the frequencies are unstable over a larger streamwise distance. Similarly, the growth rates for Case 3 are much larger than for Case 5 and the unstable range is larger for Case 3. For this case, real gas effects increase the disturbance growth rate as well as increase the unstable range of the disturbance.

VII. Conclusion

The effects of surface ablation on the instability of a real and ideal gas hypersonic boundary layer has been studied using linear stability theory. Before studying the instability physics, a thermochemical nonequilibrium linear stability theory code with carbon species due to graphite ablation and a linearized surface ablation model was developed and validated. The derivation of the linear stability theory coefficient matrices follows the work of Hudson. An eleven species gas model was used where five species model air and six more species are used to model graphite ablation effects. The derivative operators were discretized using Lagrange polynomials in physical space where for a five point stencil the order of error was shown to be four. A linearized surface ablation model applicable to parallel and non-parallel flows is given. A grid convergence study was performed to determine the required number of grid points required in the linear stability calculations. The code was then validated with results from a direct numerical simulation of flow field disturbances over a blunt cone. The comparison of the eigenfunction amplitudes as well as the streamwise wavenumbers and growth rates were good. As direct numerical simulation and linear stability theory are two dramatically different methods to analyze linear instabilities in a boundary layer the good agreement obtained between the methods lends strong confidence to their correct implementation.

To study hypersonic boundary layer instability physics five meanflow simulations were run using a high-order shock-fitting direct numerical simulation code for a 7^o half angle blunt cone at Mach 15.99. Grid convergence of the meanflows has been shown in previous research. The meanflows were devised so that effects of a real gas, blowing, and carbon species on hypersonic boundary layer instability could be isolated and analyzed. N factors for different unstable frequencies and their corresponding growth rates were computed. It was shown that changing the temperature perturbation boundary condition for an ablative flow has a strong effect on boundary layer instability. For these freestream conditions, real gas effects are strongly destabilizing. The amplification rates are higher and the instability zones are longer for a real gas. Carbon species are slightly destabilizing manifested by an increasing amplification factor. Blowing was seen to be slightly destabilizing for a real gas but its effect was negligible on an ideal gas. As a consequence to these results, a real gas should be considered in transition prediction for vehicles with ablative surfaces. If a real gas is not considered the estimated transition location may be severely overpredicted.

VIII. Future Work

Future work for the current blunt cone cases includes running the unsteady DNS simulations for the five species real gas meanflows cases. Future work for the LST code includes adding the transverse and streamwise curvature metrics to more accurately account for axisymmetric and blunt geometries respectively. For both codes future work includes updating the gas phase chemistry models with up to date forward reaction rates and equilibrium constants. In the future we would like to study how ablation affects boundary layer transition on a sphere and specifically the effects on three dimensional boundary layer instabilities.

Acknowledgements

The research was supported in part by the AFOSR/NASA National Center for Hypersonic Research in Laminar-Turbulent Transition and also the Department of Defense (DoD) through the National Defense Science & Engineering Graduate Fellowship (NDSEG) Program. The computations were run partly on XSEDE resources provided by TACC under grant number TG-ASC100002 supported in part by the National Science Foundation. Also, this work was supported in part by a grant of computer time from the DOD High Performance Computing Modernization Program at the AFRL DSRC. The views and conclusions contained herein are those of the authors and should not be interpreted as necessarily representing the official policies or endorsements either expressed or implied, of the Air Force Office of Scientific Research or the U.S. Government.

References

[1]Ungar, E., "Ablation Thermal Protection Systems," *Science*, Vol. 158, No. 3802, 1967, pp. 740–744.

[2]Mack, L., "Boundary Layer Linear Stability Theory," AGARD report No. 709, 1984.

[3]Malik, M., "Numerical Methods for Hypersonic Boundary Layer Stability," *Journal of Computational Physics*, Vol. 86, No. 2, 1990, pp. 376–413.

[4]Chang, C., Vinh, H., and Malik, M., "Hypersonic Boundary-Layer Stability with Chemical Reactions," *AIAA 1997-2012*, 1997.

[5]Stuckert, G. and Reed, H., "Linear Disturbances in Hypersonic, Chemically Reacting Shock Layers," *AIAA Journal*, Vol. 32, No. 7, 1994, pp. 1384–1393.

[6]Hudson, M., Chokani, N., and Candler, G., "Linear Stability of Hypersonic Flow in Thermochemical Nonequilibrium," *AIAA Journal*, Vol. 35, No. 6, 1997, pp. 958–964.

[7]Hudson, M., *Linear Stability Theory of Hypersonic, Chemically Reacting Viscous Flow*, Ph.D. thesis, North Carolina State University, 1996.

[8]Johnson, H., Seipp, T., and Candler, G., "Numerical Study of Hypersonic Reacting Boundary Layer Transition on Cones," *Physics of Fluids*, Vol. 10, No. 10, 1998, pp. 2676–2685.

[9]Ma, Y. and Zhong, X., "Receptivity to Freestream Disturbances of a Mach 10 Nonequilibrium Reacting Oxygen Flow over a Flat Plate," *AIAA 2004-0256*, 2004.

[10]Johnson, H., Gronvall, J., and Candler, G., "Reacting Hypersonic Boundary Layer Stability with Blowing and Suction," *AIAA 2009-938*, 2009.

[11]Ghaffari, S., Marxen, O., Iaccarino, G., and Shaqfeh, E., "Numerical Simulations of Hypersonic Boundary-layer Instability with Wall Blowing," *AIAA 2010-706*, 2010.

[12]Li, F., Choudhari, M., Chang, C., and White, J., "Boundary Layer Transition over Blunt Hypersonic Vehicles Including Effects of Ablation-Induced Out-Gassing," *AIAA 2011-3303*, 2011.

[13]Mortensen, C. and Zhong, X., "Numerical Simulation of the Effects of Graphite Ablation on Hypersonic Boundary Layer Stability," *AIAA paper 2012-3150*, 2012.

[14]Mortensen, C. and Zhong, X., "Numerical Simulation of Graphite Ablation Induced Outgassing Effects on Hypersonic Boundary Layer Receptivity over a Cone Frustum," *AIAA paper 2013-0522*, 2013.

[15]Wang, X. and Zhong, X., "A High-Order Shock-Fitting Non-Equilibrium Flow Solver for DNS of Srong Shock and Turbulence Interactions," *Seventh International Conference on Computational Fluid Dynamics*, ICCFD7-2307, 2012.

[16]Prakash, A., Parsons, N., Wang, X., and Zhong, X., "High-order Shock-fitting Methods for Hypersonic Flow with Chemical and Thermal Nonequilibrium," *AIAA 2010-4997*, 2010.

[17]Park, C., *Nonequilibrium Hypersonic Aerothermodynamics*, John Wiley & Sons Inc., New York, 1990.

[18]Dolton, T., Maurer, R., and Goldstein, H., "Thermodynamic Performance of Carbon in Hyperthermal Environments," *AIAA 68-754*, 1968.

[19]McBride, B., Heimel, S., Ehlers, J., and Gordon, S., "Thermodynamic Properties to 6000° for 210 Substances Involving the First 18 Elements," NASA SP-3001, NASA, 1963.

[20]Park, C., "On Convergence of Computation of Chemically Reacting Flows," *AIAA 85-0247*, 1985.

[21]Bhutta, B. and Lewis, C., "Low-to-High Altitude Predictions of Three-Dimensional Ablative Reentry Flowfields," *AIAA 92-0366*, 1992.

[22]Park, C., Howe, J., Jaffe, R., and Candler, G., "Chemical-Kinetic Problems of Future NASA Missions," *AIAA 91-0464*, 1991.

[23]Lee, J., "Basic Governing Equations for the Flight Regimes of Aeroassisted Orbital Transfer Vehicles," *Thermal Design of Aeroassisted Orbital Transfer Vehicles*, edited by H. F. Nelson, Vol. 96, AIAA, New York, 1985, pp. 3–53.

[24]Blottner, F., Johnson, M., and Ellis, M., "Chemically Reacting Gas Viscous Flow Program for Multi-Component Gas Mixtures," SC-RR-70-754, Sandia National Laboratories, 1971.

[25]Gupta, R., Lee, K., and Sutton, K., "Viscous-Shock-Layer Solutions with Coupled Radiation and Ablation Injection for Earth Entry," *AIAA 90-1697*, 1990.

[26]Candler, G., "Computation of Thermo-Chemical Nonequilibrium Martian Atmospheric Entry Flow," *AIAA 90-1695*, 1990.

[27]Wilke, C., "A Viscosity Equation for Gas Mixtures," *The Journal of Chemical Physics*, Vol. 18, No. 4, 1950, pp. 517–519.

[28]Zhong, X., "High-Order Finite-Difference Schemes for Numerical Simulation of Hypersonic Boundary-Layer Transition," *Journal of Computational Physics*, Vol. 144, No. 2, 1998, pp. 662–709.

[29]Prakash, A., Parsons, N., Wang, X., and Zhong, X., "High-order Shock-fitting Methods for Direct Numerical Simulation of Hypersonic Flow with Chemical and Thermal Nonequilibrium," *Journal of Computational Physics*, Vol. 230, No. 23, 2011, pp. 8474–8507.

[30]Klentzman, J., Ulker, E., and Tumin, A., "Projection of the Solution of the Linearized Navier-Stokes Equations in Reacting High Speed Boundary Layers onto Discrete Modes," *AIAA 2012-3149*, 2012.

[31]Chang, C.-L., "Langley Stability and Transition Analysis Code (LASTRAC) Version 1.2 User Manual," NASA TM-2004-213233, NASA, 2004.

[32]Anderson, E., Bai, Z., Bischof, C., Blackford, S., Demmel, J., Dongarra, J., Du Croz, J., Greenbaum, A., Hammarling, S., McKenney, A., and Sorensen, D., *LAPACK Users' Guide*, Society for Industrial and Applied Mathematics, Philadelphia, PA, 3rd ed., 1999.

[33]Park, C., "Effects of Atomic Oxygen on Graphite Ablation," *AIAA Journal*, Vol. 14, No. 11, 1976, pp. 1640–1642.

[34]Baker, R., "Graphite Sublimation Chemistry Nonequilibrium Effects," *AIAA Journal*, Vol. 15, No. 10, 1977, pp. 1391–1397.

[35]Palmer, H. and Mordecai, S., *Chemistry and Physics of Carbon*, Marcel Dekker, Inc., NY, 1968.

[36]Stuckert, G., *Linear Stability Theory of Hypersonic, Chemically Reacting Viscous Flow*, Ph.D. thesis, Arizona State University, 1991.

[37]Stetson, K., Thompson, E., Donaldson, J., and Siler, L., "Laminar Boundary Layer Stability Experiments on a Cone at Mach 8, Part 2: Blunt Cone," *AIAA 84-0006*, 1984.